Sea Surface Elevation and Bottom Pressure Anomalies due to Thermohaline Forcing. Part I: Isolated Perturbations*

RUI XIN HUANG

Department of Physical Oceanography, Woods Hole Oceanographic Institution, Woods Hole, Massachusetts

XIANGZE JIN

Department of Physical Oceanography, Woods Hole Oceanographic Institution, Woods Hole, Massachusetts, and LASG, Institute of Atmospheric Physics, Chinese Academy of Sciences, Beijing, China

(Manuscript received 8 August 2000, in final form 11 December 2001)

ABSTRACT

Sea surface elevation and bottom pressure anomalies due to thermohaline forcing are examined through analytical and numerical models, including Boussinesq and non-Boussinesq models. It is shown that Boussinesq approximations can introduce noticeable errors, depending on the spatial and temporal scales of the perturbations. According to the theory of geostrophic adjustment, when the initial perturbations have horizontal scales comparable to the barotropic radius of deformation, the initial pressure perturbations will be basically retained through the adjustment. On the other hand, if the initial perturbations have horizontal scales much smaller than the barotropic radius of deformation, the initial pressure perturbations will be largely lost. Precipitation has horizontal scales on the order of 10–100 km, much smaller than the barotropic radius of deformation. Thus, for timescales longer than days, the contribution from individual precipitation events to the local free surface elevation and bottom pressure is small and is difficult to identify from satellite data. On the other hand, thermal forcing has horizontal scales comparable to the barotropic radius of deformation, so its long-term contribution to sea surface height anomaly is noticeable and is easily identified from satellite data. Because Boussinesq models induce faulty sea surface height and bottom pressure signals, the errors introduced by these models are noticeable for anomalies in large-scale [O(1000 km)] thermohaline forcing.

1. Introduction

Boussinesq (1903) first introduced certain approximations that have been widely used in oceanic circulation models. The Boussinesq approximations can be summarized by two points. 1) The fluctuations of density are primarily due to thermohaline effects (Boussinesq's original study was focused on the contribution due to thermal forcing, as opposed to pressure; however, this assumption has been extended to include also the dynamic effect of salinity). 2) In the momentum and mass conservation equations, density variations may be neglected, except in the terms associated with buoyancy force. Thus, most existing numerical circulation models use volume conservation to replace mass conservation and use a fixed-value reference density to replace in situ density in the horizontal momentum equations.

The applicability of the Boussinesq approximations to fluid dynamics has been discussed in many papers. Spiegel and Veronis (1960) discussed the case for polytropic gases, and its application to liquids has been discussed by many other authors, such as Mihaljan (1962), Zeytounian (1989), and Bois (1991). Most of these studies have been based on nonrotating fluid; the possible dynamic effect of rotation has not been studied thoroughly.

In this study, we will emphasize that the errors in the oceanic circulation induced by Boussinesq approximations vary greatly, depending on the spatial and temporal scales of perturbations. In actuality, in the ocean both the sea level and bottom pressure may go through geostrophic adjustment processes that are very different in comparison with a Boussinesq ocean.

In the ocean, for example, the sea level increases in direct response to local heating, but there is no initial perturbation in bottom pressure. On the other hand, in a Boussinesq ocean, surface heating induces a loss of mass (thus, a negative bottom pressure signal), with no immediate increase in sea level. Because most existing

* Woods Hole Oceanographic Institution Contribution Number 10360.

Corresponding author address: Rui Xin Huang, Dept. of Physical Oceanography, Woods Hole Oceanographic Institution, Woods Hole, MA 02543.
E-mail: rhuang@whoi.edu

oceanic general circulation models are based on the Boussinesq approximations, the main concern is focused on the sea surface elevation and bottom pressure calculated from these models. To overcome this difficulty of nonconservation of mass associated with these models, a globally uniform adjustment of sea surface is needed (Greatbatch 1994). In a similar way, a correction is needed for the bottom pressure (Ponte 1999). Such global corrections have been used in many studies based on Boussinesq models, for example, Mellor and Ezer (1995) and Dukowicz (1997).

Greatbatch (1994) neglected the contribution due to local expansion of the water column, the Q' term in his Eq. (19); thus, his discussion is mostly limited to the global-mean sea level change but ignores the spatial variability in sea surface elevation and velocity. Dukowicz (1997) made an effort to improve the steric sea level calculation in the Los Alamos Parallel Ocean Program (POP) model. Although his modified model includes corrections to sea surface elevation and baroclinic velocity, such a correction does not deliver a complete correction. Because the tracer equations are based on a constant reference density, density conservation is not exact, so the model is not strictly mass conserving. Furthermore, the fixed-value reference density is used in both the horizontal momentum equations. Therefore, the model is not truly non-Boussinesq. Mellor and Ezer (1995) presented a non-Boussinesq model in sigma coordinates. By comparing experiments with idealized heating and cooling, they came to the conclusion that the differences between the non-Boussinesq and Boussinesq models are minor, when the latter was corrected by a spatially uniform, time-dependent factor calculated from the volume-averaged density change. They did not, however, compare the results from the two models driven by realistic data.

As will be shown in this study, however, the globally uniform correction to the sea surface elevation and bottom pressure may not provide an accurate description of the temporal and spatial evolution of sea surface and bottom pressure. The errors are introduced whenever density changes, because the Boussinesq approximations induce a faulty source of mass and pressure perturbations. The geostrophic adjustment in the ocean is a nonlinear process that involves complicated nonlinear interactions between mass, pressure, and velocity fields. Thus, to understand the dynamic effects induced by the density anomaly it is important to simulate the whole adjustment process accurately.

In this study we will first formulate the basic equations used in our numerical simulation and analysis in section 2. The estimate of the potential errors introduced by the Boussinesq approximations, using geostrophic scaling, is presented in section 3. The differences between the Boussinesq models and the compressible models are examined using the theory of geostrophic adjustment in section 4; these results are compared with the results from numerical experiments in section 5. Conclusions are drawn in section 6.

2. Basic equations

a. A pressure coordinates oceanic model

In this study we will compare the results from theoretical analysis and numerical experiments that were obtained from the Pressure Coordinates Oceanic Model (PCOM) that is based on pressure-σ coordinates, which are defined as

$$\sigma = \frac{p - p_t}{p_{bt}}, \qquad p_{bt} = p_b - p_t,$$

where p_b is the bottom pressure and p_t is the atmospheric pressure at the sea surface, so $\sigma = 0$ at sea surface and $\sigma = 1$ at the bottom. The pressure-σ coordinate is a vertical coordinate scaled by the bottom pressure, so the model is basically a terrain-following model.

The advantage of using pressure coordinates is that the mass conservation equation in pressure coordinates has a simple form resembling that for an incompressible fluid, so a model exactly conserving mass is relatively easy to build. The details of the model formulation can be found in a separate publication by Huang et al. (2001), and a concise description of this model is included here. The main features of the model include 1) exact mass conservation; 2) use of the in situ density ρ, instead of ρ_0 (a fixed-value reference density), in the horizontal momentum equations and the prognostic equations for the tracers; and 3) use of the accurate equation of state—thus, density is calculated using $\rho = \rho(\theta, S, P)$, where θ is potential temperature, S is salinity, and P is pressure.

The numerical calculation is carried out in double precision. The prognostic equations in spherical coordinates are

$$\frac{\partial U}{\partial t} + M(U) = f^*V - \frac{\sqrt{p_{bt}}}{a\cos\varphi}\left(\frac{\partial \phi}{\partial \lambda} + \frac{1}{\rho}\frac{\partial p}{\partial \lambda}\right) + \sqrt{p_{bt}}D_u,$$

$$\frac{\partial V}{\partial t} + M(V) = -f^*U - \frac{\sqrt{p_{bt}}}{a}\left(\frac{\partial \phi}{\partial \theta} + \frac{1}{\rho}\frac{\partial p}{\partial \theta}\right) + \sqrt{p_{bt}}D_v,$$

$$\frac{\partial p_{bt}}{\partial t} + L(p_{bt}) = 0,$$

$$\frac{\partial p_{bt}\theta}{\partial t} + L(p_{bt}\theta) = p_{bt}Q_\theta,$$

$$\frac{\partial p_{bt}S}{\partial t} + L(p_{bt}S) = p_{bt}Q_S,$$

where $f^* = 2\Omega\sin\varphi + u\tan\varphi/a$ is the apparent Coriolis parameter; $(U, V) = (\sqrt{p_{bt}}u, \sqrt{p_{bt}}v)$ are the pressure-

TABLE 1. Differences between a mass-conserving model (PCOM) and the Boussinesq Compromised Ocean Model (BCOM).

	PCOM	BCOM	Error bound in BCOM
Continuity equation	$\frac{D\rho}{Dt} + \rho\nabla\cdot\mathbf{u} = 0$	$\nabla\cdot\mathbf{u} = 0$	1%
Momentum equations	$\frac{Du}{Dt} = f^*v - \frac{1}{a\rho\cos\varphi}\frac{\partial p}{\partial\lambda} + D_u$	$\frac{Du}{Dt} = f^*v - \frac{1}{a\rho_0\cos\varphi}\frac{\partial p}{\partial\lambda} + D_u$	1%–2%
Tracer equations	$\frac{D\rho\theta}{Dt} + \nabla\cdot(\rho\mathbf{u}\theta) = Q_\theta$	$\frac{D\rho_0\theta}{Dt} + \nabla\cdot(\rho_0\mathbf{u}\theta) = Q_\theta$	1%
Equation of state	$\rho = \rho(\theta, S, P)$	$\rho = \rho(\theta, S, \rho_0 gh)$	0.1%

weighted horizontal velocities; M and L are the advection operators

$$M(\mu) = \frac{1}{a\cos\varphi}\left(\frac{\partial u\mu}{\partial\lambda} - \frac{\mu}{2}\frac{\partial u}{\partial\lambda} + \frac{\partial v\cos\varphi\mu}{\partial\theta} - \frac{\mu}{2}\frac{\partial v\cos\varphi}{\partial\theta}\right) + \left(\frac{\partial\dot\sigma\mu}{\partial\sigma} - \frac{\mu}{2}\frac{\partial\dot\sigma}{\partial\sigma}\right)$$

$$L(\mu) = \frac{1}{a\cos\varphi}\left(\frac{\partial\mu u}{\partial\lambda} + \frac{\partial\mu v\cos\varphi}{\partial\theta}\right) + \frac{\partial\mu\dot\sigma}{\partial\sigma};$$

and D_u, D_v, Q_θ, and Q_S represent turbulent viscosity and mixing.

The geopotential height is calculated based on the hydrostatic approximation:

$$\phi = gz_b + \int_\sigma^1 \frac{p_{bt}}{\rho}\,d\sigma,$$

where z_b is the sea floor and the in situ density is calculated using the new version of the equation of state $\rho = \rho(\theta, S, p)$, where θ is the potential temperature (Jackett and McDougall 1995).

The boundary conditions include the following: At all sidewalls and the bottom, the velocity is zero, and there is no heat or salt flux. At the free surface ($\sigma = 0$), the kinematic boundary conditions are

$$p_{bt}\dot\sigma = -\rho_f g(e - p) \quad \text{and} \quad \frac{\rho^2 g}{p_{bt}}A_v\frac{\partial\mathbf{u}}{\partial\sigma} = -\tau,$$

where $(e - p)$ is the rate of evaporation minus precipitation combined with river runoff, ρ_f is the density of freshwater; and τ represents wind stress. The turbulent mixing for temperature at the sea surface is

$$\frac{\rho^2 g}{p_{bt}}\kappa_v\frac{\partial\theta}{\partial\sigma} = -\frac{F_h}{C_p},$$

where κ_v is the vertical diffusivity, F_h is the air–sea heat flux and C_p is the heat capacity of seawater. The natural boundary condition for salinity (Huang 1993) is that the turbulent salt flux is exactly canceled by the salt advection:

$$\frac{\rho^2 g}{p_{bt}}\kappa_v\frac{\partial S}{\partial\sigma} = -S_s\rho_f(e - p),$$

where S_s is salinity in the upper layer, and the freshwater from precipitation minus evaporation enters the ocean as a mass flux through the continuity equation.

b. A Boussinesq compromised oceanic model

To see the errors introduced by the Boussinesq approximations, we construct a second model called BCOM (Boussinesq Compromised Oceanic Model). The details of the model formulation can be found in a separate publication by Huang et al. (2001). This model is based on the traditional Boussinesq approximations and sigma coordinates; it has almost the identical coding structure as PCOM, except for some minimal changes listed in Table 1.

c. Sea surface elevation in a compressible ocean model

The mass conservation law is

$$\frac{\partial u}{\partial x} + \frac{\partial v}{\partial y} + \frac{\partial w}{\partial z} = -\frac{1}{\rho}\frac{D\rho}{Dt} = \alpha\frac{D\theta}{Dt} - \beta\frac{DS}{Dt} - \gamma\frac{Dp}{Dt}, \quad (1)$$

where $\alpha = -(1/\rho)(\partial\rho/\partial\theta)|_{s,p}$ and $\beta = (1/\rho)(\partial\rho/\partial S)|_{\theta,p}$ are the heat expansion and salt contraction coefficients and $\gamma = 1/(\rho c_s^2)$ where c_s is the speed of sound. The surface boundary conditions have been discussed in previous studies, for example, Wolfgang (1973) and Huang (1993):

$$w = \frac{\partial\eta}{\partial t} + \mathbf{u}\cdot\nabla\eta + (e - p)\frac{\rho_f}{\rho_s};$$

$$\kappa_v\frac{\partial\theta}{\partial z} - \kappa_h\nabla_h\theta\cdot\nabla\eta = \frac{\alpha_s}{\rho_s C_p}F_H;$$

$$\kappa_v\frac{\partial S}{\partial z} - \kappa_h\nabla_h S\cdot\nabla\eta = (e - p)\frac{\rho_f}{\rho_s}S_s;$$

where ρ_s is the sea surface density and F_H is the sea surface heat flux. The lower boundary conditions are

$$w = -\mathbf{u}\cdot\nabla H;$$

$$\kappa_v\frac{\partial\theta}{\partial z} - \kappa_v\nabla_h\theta\cdot\nabla(-H) = 0;$$

$$\kappa_v\frac{\partial S}{\partial z} - \kappa_v\nabla_h S\cdot\nabla(-H) = 0.$$

Using the vertical boundary conditions, integrating Eq. (1) leads to

$$\frac{\partial \eta}{\partial t} = -\left(\frac{\partial}{\partial x}\int_{-H}^{\eta} u\, dz + \frac{\partial}{\partial y}\int_{-H}^{\eta} v\, dz\right) - (e - p)\frac{\rho_f}{\rho_s} + \int_{-H}^{\eta}\left(\alpha\frac{D\theta}{Dt} - \beta\frac{DS}{Dt} - \gamma\frac{Dp}{Dt}\right) dz.$$

The salinity term is

$$\int_{-H}^{\eta}\beta\frac{DS}{Dt}\,dz = \int_{-H}^{\eta}\beta\left(\kappa_v\frac{\partial S}{\partial z}\right)dz + \int_{-H}^{\eta}\beta\nabla_h\cdot(\kappa_h\nabla_h S)\,dz = (e - p)\frac{\rho_f}{\rho_s}\beta_s S_s + \nabla_h\cdot\int_{-H}^{\eta}\beta\kappa_h\nabla_h S\,dz - \text{CABS},$$

where CABS represents the cabbeling effect:

$$\text{CABS} = \int_{-H}^{\eta}\kappa_v\frac{\partial S}{\partial z}\frac{\partial\beta}{\partial z}\,dz + \int_{-H}^{\eta}\kappa_h\nabla_h S\cdot\nabla_h\beta\,dz.$$

In a similar way, we have

$$\int_{h}^{\eta}\alpha\frac{D\theta}{Dt}\,dz = \frac{\alpha_s}{\rho_s c_p}F_H + \nabla_h\cdot\int_{-H}^{\eta}\kappa_h\nabla_h\theta\,dz + \text{CABT},$$

and

$$\text{CABT} = -\int_{-H}^{\eta}\kappa_v\frac{\partial\theta}{\partial z}\frac{\partial\alpha}{\partial z}\,dz - \int_{-H}^{\eta}\kappa_h\nabla_h\theta\cdot\nabla_h\alpha\,dz.$$

If we neglect the small correction term due to pressure changes, the free surface elevation equation is

$$\frac{\partial\eta}{\partial t} = -\left(\frac{\partial}{\partial x}\int_{-H}^{\eta}u\,dz + \frac{\partial}{\partial y}\int_{-H}^{\eta}v\,dz\right) - (e - p) + \frac{\alpha_s}{\rho_s c_p}F_H + \nabla_h\cdot\int_{-H}^{\eta}\kappa_h\nabla_h\theta\,dz - \nabla_h\cdot\int_{-H}^{\eta}\beta\kappa_h\nabla_h S\,dz + \text{CABT} + \text{CABS}. \quad (2)$$

The pressure term

$$\int_{-h}^{\eta}\gamma\frac{Dp}{Dt}\,dz = \gamma\int_{-H}^{\eta}\frac{D}{Dt}\int_{z}^{\eta}\rho g\,dz\,dz + \gamma\int_{-H}^{\eta}\frac{Dp_t}{Dt}\,dz \cong g\gamma\int_{-H}^{\eta}\left(\rho_s\frac{\partial\eta}{\partial t} - \rho w + \int_{z}^{\eta}\frac{D\rho}{Dt}\,dz\right)dz + \gamma(\eta + H)\frac{Dp_t}{Dt} \cong \frac{\Delta\rho}{\rho_0}\left(\frac{\partial\eta}{\partial t} + \int_{-H}^{\eta}\frac{1}{\rho}\frac{D\rho}{Dt}\,dz + \frac{1}{\rho_0 g}\frac{Dp_t}{Dt}\right),$$

where $\Delta\rho/\rho_0 = \gamma(\eta + H)\rho_0 g \approx (\rho_b - \rho_s)/\rho_0 \approx 3\%$ (ρ_0 is the fixed-value reference density), and the vertical integration of the w term is discarded because it is far less than the η term. In addition,

$$\gamma g\int_{-H}^{\eta}\int_{z}^{\eta}\frac{D\rho}{Dt}\,dz\,dz = \gamma g\int_{-H}^{\eta}\frac{D\rho}{Dt}(z + H)\,dz \approx \frac{\Delta\rho}{\rho_0}\int_{-H}^{\eta}\frac{1}{\rho}\frac{D\rho}{Dt}\,dz.$$

Last we have

$$\frac{\partial\eta}{\partial t} = -\left[\frac{\partial}{\partial x}\int_{-H}^{\eta}u\,dz + \frac{\partial}{\partial y}\int_{-H}^{\eta}v\,dz + (e - p)\right]\left(1 - \frac{\Delta\rho}{\rho_0}\right) + \frac{\alpha_s}{\rho_s c_p}F_H + \nabla_h\cdot\int_{-H}^{\eta}\kappa_h\nabla_h\theta\,dz - \nabla_h\cdot\int_{-H}^{\eta}\beta\kappa_h\nabla_h S\,dz + \text{CABT} + \text{CABS} - \frac{\Delta\rho}{\rho_0^2 g}\frac{Dp_t}{Dt}. \quad (3)$$

3. Errors introduced by the Boussinesq approximations

To determine the errors introduced by the Boussinesq approximations, we estimate the possible errors by geostrophic scaling. First, we begin with the errors introduced in the mass conservation equation by the volume conservation approximation. Using the geostrophic approximation for global scales, the density field can be nondimensionalized as $\rho = \rho_0 + [(\rho_0 fUL)/(gD)]\rho'$, where ρ_0 is the fixed-value reference density, f is the Coriolis parameter, U is the velocity, L and D are the horizontal and vertical length scales, and ρ' is the nondimensional density. The continuity equation can be reduced to the following nondimensional form (Pedlosky 1987):

$$R_o F\frac{D\rho'}{Dt'} + (1 + R_o F\rho')\nabla'\cdot\mathbf{u}' = 0, \quad (4)$$

where $R_o = U/(fL)$ is the Rossby number and $F = (f^2L^2)/(gD)$, $t' = tU/L$, $\nabla' = \nabla/L$, and $\mathbf{u}' = \mathbf{u}/U$ is the nondimensional velocity. If R_oF is extremely small or equal to zero, the assumption of volume conservation is a good approximation. On the other hand, if R_oF is not very small, the errors introduced by the volume conservation approximation are not negligible. Because $R_oF = (UfL)/(gD)$, we expect that the errors introduced by neglecting the density change terms will be large when

1) U is large—fast current, such as the Gulf Stream or the Antarctic Circumpolar Current;
2) f is large—at high latitudes;

3) L is large—large-scale phenomena, such as heating or cooling over a large portion of the ocean; or
4) D is small—where the motion is confined to a relatively thin layer in the upper ocean.

As an example, we apply this estimate for global-scale motion, so $L = r_0 = 6400$ km is the radius of the earth and $f = 2\Omega$ (Ω is the angular velocity of the earth's rotation). Assuming the horizontal velocity scale of $U = 10$ cm s^{-1} and the depth scale of the motion $D = 800$ m, we have $R_o \approx 10^{-4}$ and $F \approx 100$; thus, replacing the mass conservation with the volume conservation can introduce errors of about 1%.

Second, the errors introduced by replacing the in situ density with the fixed-value reference density in the horizontal momentum equations are about 1%–2% because the range of in situ density variation in the ocean is about 3%.

Note that the above estimate is for the instantaneous errors only. Because these errors are not random, they can accumulate and lead to much larger errors after a long-time integration of the models.

In this study, we will focus primarily on the free surface elevation and bottom pressure, although errors also appear in other dynamic variables, such as horizontal velocity. The time evolution of sea surface elevation (compressibility terms are neglected here) is described by Eq. (2). Thus, the time evolution of surface elevation is controlled by

1) divergence of the barotropic velocity, the first term on the right-hand side;
2) evaporation minus precipitation, the $e - p$ term;
3) surface heating, the F_H term; and
4) cabbeling, the remaining terms.

Although in this equation these contributions are listed separately, the long-time contribution to the sea surface elevation from individual terms at a fixed location is not obvious. In fact, sea surface elevation is controlled by the complicated nonlinear dynamic processes, in which all these factors combine. As a result, for timescales longer than days, the sea surface elevation at a given station due to these forcing terms cannot be simply inferred from this equation. For example, as the solution approaches a quasi equilibrium, the time rate of the sea surface elevation vanishes, and there are no other terms in this equation that can be used for predicting the sea surface elevation at a steady state. Thus, it is important to examine the contributions from all terms in this equation to understand the time evolution of the sea surface elevation. In particular, the barotropic velocity convergence term leads to lateral mass exchanges and thus plays an important role in setting up the sea surface elevation. In accord, sea surface elevation changes on longer timescales are directly related to the geostrophic adjustment processes, which will be discussed shortly.

Although many studies have been focused on the sea surface elevation obtained from either numerical models or satellite observations, there are few theoretical analyses devoted to the evolution of sea surface elevation on long timescales. For example, Greatbatch (1994) gave a concise analysis for sea level changes diagnosed from Boussinesq models, and his argument has been cited as the theoretical background in many studies related to sea surface elevation changes diagnosed from satellite data. Greatbatch estimated that the contribution to sea level increase from evaporation minus precipitation is much larger than that from thermal forcing. However, sea surface elevation anomalies identified from satellite data often show a strong relation between the thermal forcing anomalies, but they seldom show any contribution from local evaporation minus precipitation. The reason for this apparent contradiction will explained in the next section.

The time evolution of bottom pressure is

$$\frac{\partial p_b}{\partial t} = \frac{\partial p_t}{\partial t} - \left(\frac{\partial}{\partial x}\int_{-H}^{\eta} \rho g u \, dz + \frac{\partial}{\partial y}\int_{-H}^{\eta} \rho g v \, dz\right) - (e - p)\rho_f g. \tag{5}$$

Thus, the time evolution of bottom pressure is controlled by

1) changes in the sea surface atmospheric pressure,
2) convergence of mass in the water column, and
3) local evaporation minus precipitation.

Similar to the dynamic processes controlling the sea surface elevation, these three factors combine through nonlinear dynamic processes and affect the time evolution of the bottom pressure at a given location. For timescales longer than days, the impact of local atmospheric pressure and evaporation minus precipitation is transformed through the geostrophic adjustment involving the current on much larger scales. Thus, the local bottom pressure signal left after geostrophic adjustment cannot be simply inferred from the individual contributors.

For the Boussinesq ocean, however, the bottom pressure equation becomes

$$\frac{\partial p_b}{\partial t} = \frac{\partial p_t}{\partial t} - \rho_0 g\left(\frac{\partial}{\partial x}\int_{-H}^{\eta} u \, dz + \frac{\partial}{\partial y}\int_{-H}^{\eta} v \, dz\right) - (e - p)\rho_f g + g\int_{-H}^{\eta} \frac{\partial \rho}{\partial t} \, dz. \tag{6}$$

In comparison with the non-Boussinesq ocean, it adds source/sink terms due to change in density. As a result, the basin-integrated bottom pressure anomaly becomes negative (positive) when the basin is warming up (cooling down). To correct for the missing physics, a simplified approach is to make a correction to the bottom pressure at each time step, using the averaged density changes over the global ocean, that is, $(g/A)\overline{\int_V (\partial\rho/\partial t)\, dV}$ (Ponte 1999).

Thus, a simple way to mend the errors introduced to

Boussinesq models is to compensate the total mass loss from heating and spread the loss of mass uniformly over the whole ocean (e.g., Greatbatch 1994; Ponte 1999). Note that the correction proposed by Greatbatch (1994) was originally intended for a quasi–steady state solution only, but it is now widely used for the time evolution of sea surface elevation, bottom pressure (Ponte 1999), and angular momentum of the oceans (Bryan 1997). The reason for applying this correction to these time-dependent problems is that, without such a correction, changes in sea surface elevation, bottom pressure, and angular momentum calculated from the Boussinesq models are almost meaningless because they are so severely contaminated with faulty signals due to the lack of mass conservation. Thus, in our study, all results obtained from the Boussinesq model (BCOM) will be subject to such a correction.

With the assumption that the global-integrated evaporation minus precipitation rate is zero, the global-mean bottom pressure correction is

$$\overline{\delta p_b} = \frac{1}{A}\iint_A \delta p_b \, dx \, dy, \tag{7}$$

where A is the total area of the model ocean and $\delta p_b = p_b - p_b^0$ is the bottom pressure deviation from the initial value p_b^0. The free surface elevation and bottom pressure, including the correction, for BCOM are

$$\eta = \eta_0 - \frac{1}{\rho_0 g}\overline{\delta p_b}, \tag{8}$$

$$p_b = p_{b,0} - \overline{\delta p_b}. \tag{9}$$

As discussed above, the spatially uniform correction may not always yield the right solutions when the scale of the perturbations is comparable to the barotropic radius of deformation.

4. Geostrophic adjustment in simple analytical models

a. The effect of surface heating and cooling

Density changes are associated with thermohaline forcing at the boundaries and mixing in the interior. In the ocean, sea surface elevation increases in response to heating, but in a Boussinesq ocean it remains unchanged initially. The initial profiles of pressure perturbation are different for these two ocean models (Fig. 1). In a compressible ocean there is a baroclinic pressure anomaly within the surface layer, but there is no pressure perturbation below the top layer. On the other hand, in a Boussinesq ocean there is a barotropic pressure anomaly; that is, the pressure anomaly linearly increases downward within the top layer, and it is constant below the top layer. As noted by a reviewer, it is interesting to note that the Boussinesq approximations interchange the roles of bottom pressure (a measure of mass) and surface elevation (a measure of volume), and this misinterpretation of the physics is the root of the errors introduced in the Boussinesq models.

The pressure perturbations in these two models drive anomalous currents, thus initializing the adjustment processes. If there is no rotation, that is, $f = 0$, the velocity change is controlled by the pressure gradient and friction. With the assumption of weak friction, the current is controlled by the pressure gradient. In the final state the light water will be uniformly spread over the entire basin, resulting in a basinwide uniform stratification. The difference between these two models is very small.

For rotating fluids, the adjustment processes are different from those in nonrotating fluids because of the Coriolis force. Now the balance in the momentum equation is between the acceleration term, the Coriolis force, the pressure gradient force, and the frictional force. For large-scale motion, friction is negligible, and the Coriolis term and the pressure term are the most important terms, dominating the evolution of the adjustment.

The geostrophic adjustment processes can be illustrated by the cartoons in Fig. 1. When water in the upper layer of a compressible ocean is heated from above, the free surface is moved upward, indicated by a slightly higher level in the middle of Fig. 1a, while the sea surface in the environment is unperturbed. The sea surface height anomaly creates a horizontal pressure gradient field. Over the depth of a water column within this patch of water, there is a positive pressure perturbation in the upper layer, with no pressure perturbation in the layer below because total mass does not change initially; see the solid line in Fig. 1c. Driven by the high pressure, the light water spreads outward. However, the Coriolis force turns this outward flow into an anticyclonic circulation in the upper layer (Fig. 1a). As the upper layer loses water, the sea level within the heated area declines slightly. A negative pressure anomaly appears in the layer below, which drives an inward flow and induces a cyclonic circulation (Fig. 1b). The pressure perturbation profile in the final state is depicted by the dotted line in Fig. 1c.

For a Boussinesq model, the adjustment processes take a different route. After the initial heating, the sea level remains unchanged because of the assumption of volume conservation, so the sea level remains flat everywhere (Fig. 1d). Since density for water in the upper box declines because of heating, there is an artificial loss of mass in the water column subject to heating. As a result, there is a negative pressure perturbation below the sea surface, and the pressure profile right after heating is indicated by the solid line in Fig. 1f. This pressure anomaly drives an inward flow within the whole water column and induces a cyclonic circulation (Fig. 1d). The inward flow raises the sea level within the heating area and thus increases the pressure within the whole water column. As a result, the subsurface pressure perturbation in the heating area becomes positive; see the dotted line in Fig. 1f. This positive pressure perturbation drives an outward flow in the upper layer and creates an anticy-

A. A Compressible Ocean

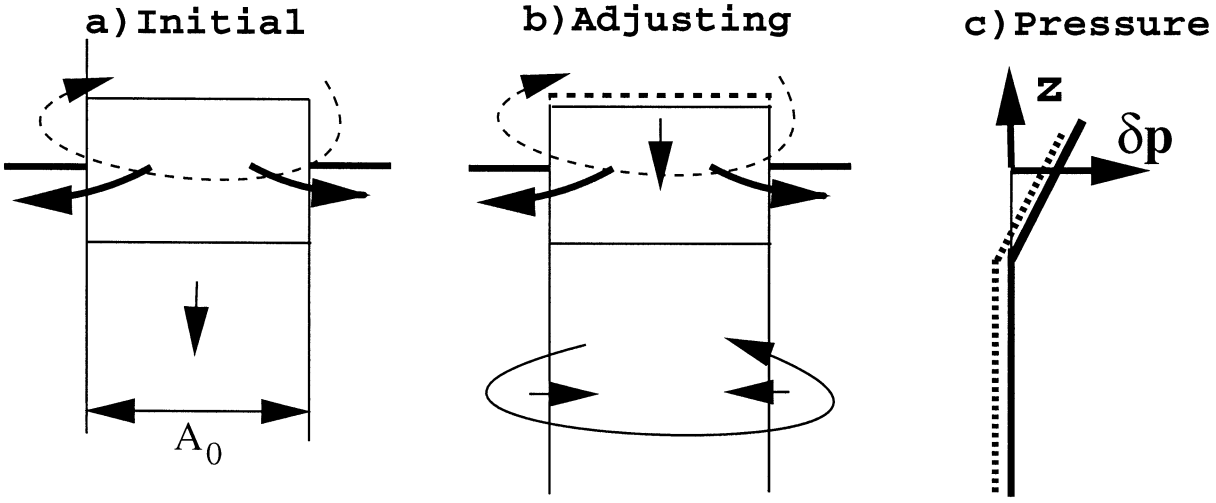

B. A Boussinesq Ocean

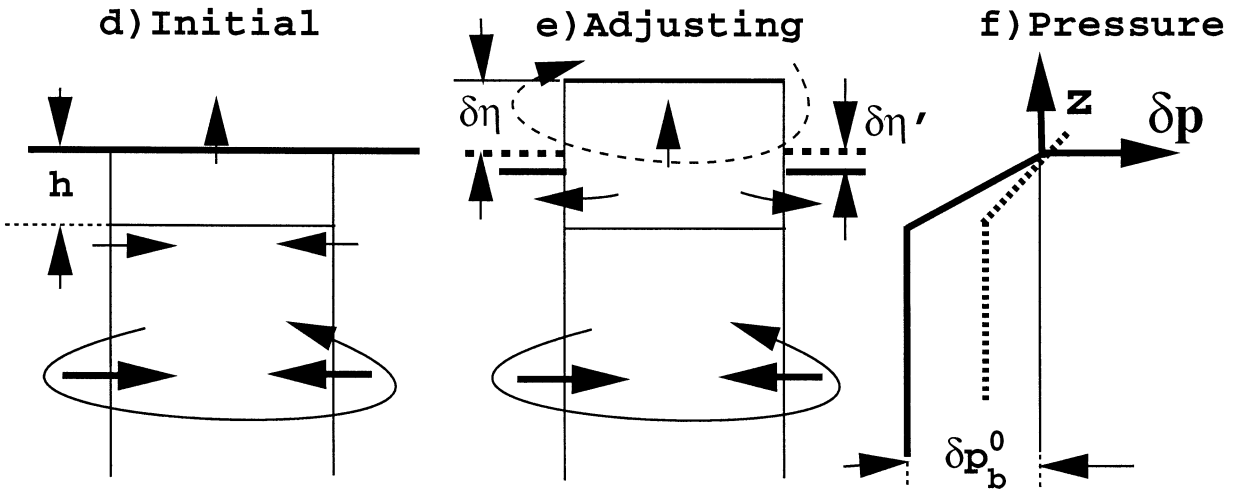

FIG. 1. Sketch of geostrophic adjustment in response to surface heating.

clonic circulation in the upper layer (Fig. 1e). Although these two models behave differently, they share the same property that the Coriolis force prevents the complete collapse of the initial pressure perturbations.

As an example, we analyze the following idealized case with surface heating on a water column (lower panel of Fig. 1). In a Boussinesq model there is a negative bottom pressure signal created during the heating, $\Delta p_b^0 = gh\delta\rho < 0$. If it is assumed that in the area of heating there is a residual bottom pressure signal, $\Delta p_b^0 < \Delta p_b < 0$, left after the geostrophic adjustment, we have

$$(H + \delta\eta')\rho_0 = (\rho_0 + \delta\rho)h + (H + \delta\eta - h)\rho_0 - \Delta p_b/g,$$

where H is the constant depth of the model ocean and $\delta\rho < 0$ is the density change from heating. This leads to

$$h(\delta\rho/\rho_0) = \delta\eta' - \delta\eta + \Delta p_b/(g\rho_0).$$

From mass conservation used in Boussinesq models,

$$A_0\delta\eta + (A - A_0)\delta\eta' = 0,$$

where A is the total area of the model basin and A_0 is the area of the perturbed water column. From these equations we obtain the following relations:

$$\delta\eta = \left(1 - \frac{A_0}{A}\right)\left(-h\frac{\delta\rho}{\rho_0} + \frac{\Delta p_b}{g\rho_0}\right) > 0,$$

$$\delta\eta' = \frac{A_0}{A}\left(h\frac{\delta\rho}{\rho_0} - \frac{\Delta p_b}{g\rho_0}\right) < 0.$$

The difference in free surface elevation between the heated water column and the environment is

$$\delta\eta - \delta\eta' = -h\frac{\delta\rho}{\rho_0} + \frac{\Delta p_b}{g\rho_0}.$$

As discussed before, whether the initial bottom pressure signal will persist through geostrophic adjustment depends on the initial horizontal scale relative to the barotropic radius of deformation and the scale of the model basin (factor A_0/A). For the case of small horizontal scale, there is very little bottom pressure signal left after the geostrophic adjustment, $\Delta p_b \approx 0$, so the free surface elevation difference between the perturbed water column and the unperturbed environment would be the same as in a compressible model. In such a case, the global correction of bottom pressure would produce the same free surface elevation as in a compressible model.

On the other hand, if the horizontal scale of heating is on the order of the radius of deformation, part of the initial bottom pressure will persist that is, $(\Delta p_b)/(g\rho_0) < 0$; thus, the results from the Boussinesq models and the compressible model differ.

The difference between the Boussinesq models and the compressible model is controlled by the dispersion of bottom pressure signals through Rossby waves during the geostrophic adjustment. Any dynamic processes that prevent the dispersion of Rossby waves can help to maintain the difference between these two types of models: 1) large horizontal scale of the initial perturbations; 2) lateral boundary; 3) strong current, such as the Gulf Stream or the Antarctic Circumpolar Current, through wave–current interaction; or 4) large-scale topography, through waves–topography interaction.

However, such phenomena are complicated, and they are left for further study. In the discussion below, we will show a case in which the dynamic role of both the large horizontal scale and the lateral boundary come into play, so that the difference between a Boussinesq model and a compressible model is noticeable, even though the global correction has been applied to the results.

The physical processes discussed above can be quantified using analytical models. A most concise way of describing the geostrophic adjustment process is to seek an analytical description of the initial state and the final state after the completion of the adjustment. Geostrophic adjustment has been a classic topic of study. In his seminal paper, Rossby (1938) concluded that the pressure field adjusted toward the velocity field. However, further studies indicated that both the velocity and pressure fields adjust, depending on the initial horizontal scale of the perturbations. For example, Yeh (1957) studied the analytical solutions of the geostrophic adjustment and pointed out that the direction of geostrophic adjustment depends on the initial horizontal scale, in comparison with the radius of deformation. If the initial perturbation has a small horizontal scale, wave processes can disperse the energy within a timescale shorter than $1/f$. Within such a short time, the vorticity field (or the velocity field) remains basically unchanged; however, the pressure field is altered to be in geostrophic balance with the velocity. On the other hand, if the initial horizontal scale is large, the adjustment processes take a much longer time, so a new velocity field is established that is in balance with the pressure gradient, and changes in the pressure field stop. As a result, the initial pressure perturbations can mostly remain unchanged.

Thus, in terms of the adjustment processes there are major differences between rotating fluids and nonrotating fluids. The existence of the Coriolis force preserves the pressure perturbations created by thermohaline forcing or mixing, and the degree of preservation of the initial pressure perturbations depends on the horizontal scale of the initial pressure perturbation as discussed below. For density perturbations due to thermohaline forcing in a one-dimensional, two-layer model on an f plane, the final state of the geostrophic adjustment can be solved in closed analytical form. The description of the analytical solution is included in the appendix. Note that although the analytical solutions are for cases with simple geometry on the f plane, they provide a solid benchmark for the numerical models.

The scalar selection of the geostrophic adjustment due to heating can be illustrated using a simple model in which the heating anomaly is initially confined to a finite domain with a radius of r_0. Assume the model ocean consists of an upper layer of 100 m and a second layer of 1000 m. After heating, the upper-layer density is reduced, so the density ratio is $\gamma = \rho_1/\rho_2 = 0.99$, and the layer-thickness ratio is $\kappa = 10$. The solutions from the compressible model (PCOM) are shown in the left panels of Fig. 2, where the horizontal axis is in units of the barotropic radius of deformation R_b. The solutions from the Boussinesq model (BCOM) are shown in the right-hand panels of Fig. 2. (Although the results presented here were obtained from analytical models with two layers, for simplicity we will use PCOM and BCOM to label them because the same solutions can be obtained from PCOM and BCOM.)

Note that when the nondimensional radius of the initial perturbation $R = r_0/R_b \geq 1$ there is a sharp front in the bottom pressure profile obtained from PCOM,

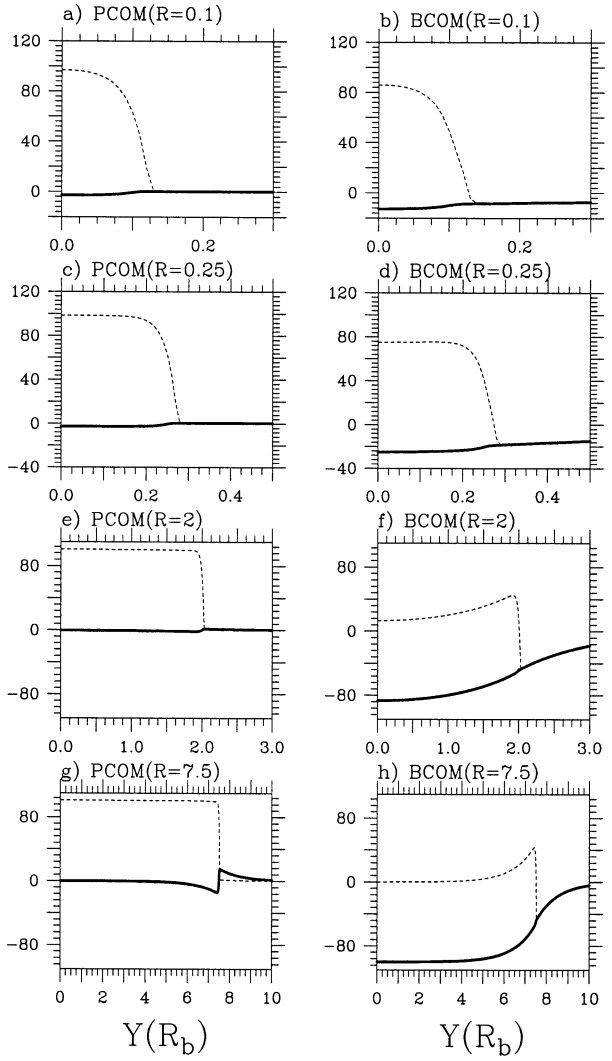

FIG. 2. Geostrophic adjustment for PCOM and BCOM for the case when heating reduces the density in the upper 100 m to $0.99\rho_0$; the lower layer density is ρ_0 and its thickness is 1000 m, and R is the radius of the initial perturbation. Here $R_b = \sqrt{gh}/f \approx 1000$ km ($h = 1.1$ km) is the barotropic radius of deformation for the ocean. Dashed lines are for the free surface elevation (cm) and solid lines are for the bottom pressure perturbations [in centimeters of water column; P_b in (g) is exaggerated 10 times to show the structure of the front].

although the bottom pressure signal itself is small. On the other hand, the bottom pressure anomaly in BCOM is big, and there is no sharp front in the bottom pressure profile.

It is clear that when the initial horizontal scale is much smaller than the barotropic radius of deformation, results from PCOM and BCOM are similar. As the initial horizontal scale becomes comparable to the barotropic radius of deformation, the difference between these two models becomes noticeable. When the perturbations have a horizontal scale on the order of the barotropic radius of deformation, the differences between these two become very large. In PCOM the initial signal of the free surface elevation will persist, and there is very little bottom pressure perturbation in the final state. On the other hand, results from BCOM indicate that the initial bottom pressure signal will persist, and there will be very little signal in the free surface elevation. These results are consistent with the theoretical reasoning discussed above.

b. Sea level and bottom pressure changes due to precipitation

Precipitation affects the ocean in a way that is very different from thermal forcing because precipitation carries a mass flux affecting salinity through dilution, and it is essentially barotropic in both the Boussinesq models and the compressible models.

The geostrophic adjustment problems associated with precipitation can be described using the analytical solution discussed in the appendix. Because precipitation induces a pressure perturbation that is barotropic in nature, only precipitation that has an initial horizontal scale comparable to the barotropic radius of deformation can persist through the geostrophic adjustment. In fact, calculations based on either the analytical models in the appendix or the numerical models PCOM or BCOM demonstrated that, for precipitation with horizontal scale smaller than the barotropic radius of deformation, weak barotropic signals in both the surface elevation and bottom pressure are left behind. Only if the precipitation has an initial horizontal scale larger than the barotropic radius of deformation, will there be strong signals in surface elevation and bottom pressure after the completion of the geostrophic adjustment. Barotropic adjustment is carried out primarily by the barotropic Rossby waves. The phase speed of the barotropic Rossby waves with a horizontal scale of 100 km is about 10 times as slow as that of the barotropic long waves. However, the ''apparent'' adjustment time remains on the order of a few days because the barotropic waves can disperse the initial perturbations over a range that is 10 times as large as the dimension of the initial perturbations.

As an example, we discuss a case with rainfall onto a semi-infinite plane. For simplicity, we include the domain near the origin only (Fig. 3). For this case the solutions from either the PCOM, the BCOM (both for cases of constant f), or the analytical model with or without the Boussinesq approximations are very close to each other. From this solution, it is readily seen that in the final state the front associated with the precipitation has a horizontal scale comparable to the barotropic radius of deformation; thus, if the precipitation has an initial scale much smaller than the barotropic radius of deformation R_b, there will be very little signal of sea level and bottom pressure anomaly left after the geostrophic adjustment. It is important to note that this solution is valid for the f plane only. On a β plane or

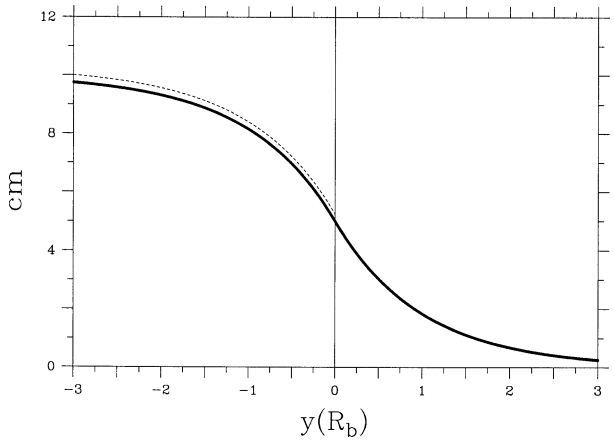

FIG. 3. Free surface elevation (dashed) and bottom pressure after adjustment in response to precipitation of 10 cm onto the left side of a semi-infinite plane in PCOM.

spherical coordinates, the front associated with the edge of the precipitation is subject to strong Rossby wave activity; see the discussion in section 5b.

The barotropic radius of deformation is approximately $R_b = \sqrt{gH_b}/f \approx 2000$ km, with the assumption that the mean depth of the ocean is $H_b = 4$ km. The precipitation from a rainstorm in the atmosphere has a horizontal scale on the order of 10–100 km, which is much smaller than the barotropic radius of deformation. Thus, sea surface elevation signals due to precipitation mostly disappear during the fast barotropic geostrophic adjustment. Although precipitation minus evaporation makes a contribution to the temporal evolution of the local sea level that is much larger than that from thermal forcing, as can be seen from Eq. (2), the sea surface elevation signals diagnosed from satellite altimeter data do not show a strong contribution from precipitation.

In addition, there is a weak baroclinic pressure signal due to the salinity change in the upper ocean induced by mixing of freshwater with the seawater. The adjustment of this baroclinic pressure signal obeys a dynamic law similar to that discussed above. Because the horizontal scale of precipitation is on the same order as the first baroclinic radius of deformation, the baroclinic pressure signal due to precipitation tends to persist during the geostrophic adjustment. The basic scales of the freshwater lens can be estimated as follows. Assume that the upper-layer thickness is H_1, with salinity of $S_0 = 35$ and density of ρ_0. Add precipitation of $\delta h \ll H_1$, and the density of the precipitated water is $\rho_f = \rho_0(1 - \beta S_0) < \rho_0$. Assume $\beta = 0.000\,67$, so $\beta S_0 \approx 0.025$. The new salinity after complete mixing is $S = S_0[(H_1\rho_0)/(H_1\rho_0 + \delta h\rho_f)]$. Thus, the perturbation in salinity is

$$\delta S = -S_0 \frac{\delta h}{H_1}\frac{\rho_f}{\rho_0} \approx -S_0\frac{\delta h}{H_1}. \quad (10)$$

The new density is $\rho = \rho_0 + \delta\rho$, where $\delta\rho = \rho_0\beta\delta S = -\rho_f\beta S_0(\delta h/H_1)$. After saline mixing, the upper layer has a thickness of $h = [(H_1 + (\delta h\rho_f/\rho_0)], [\rho_0/(\rho_0 + \delta\rho)] \approx H_1[1 + (\delta h/H_1)]$. Thus, the actual free surface after mixing remains almost unchanged at $\Delta h \approx \delta h$.

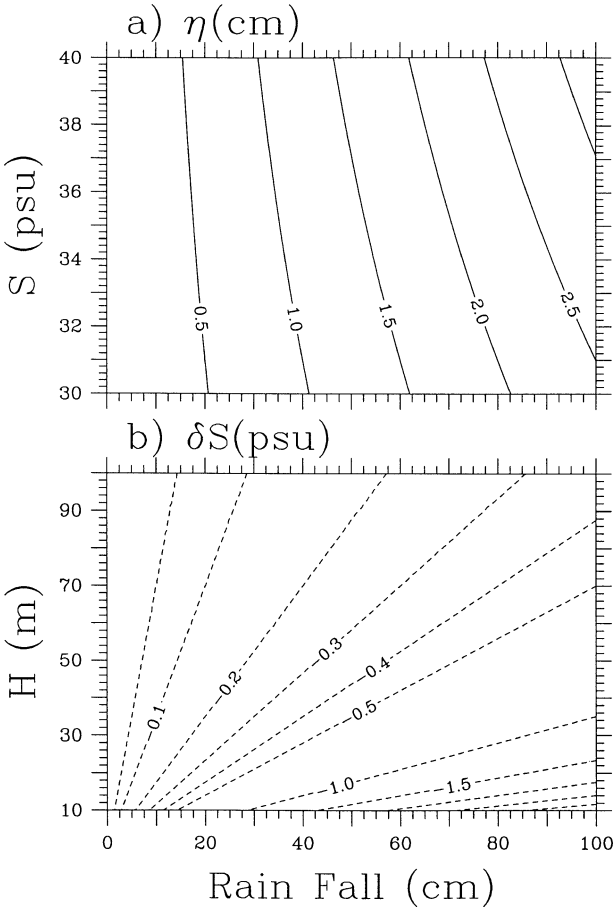

FIG. 4. Sea surface height and surface salinity anomaly from precipitation of small scales after the completion of geostrophic adjustment on an f plane. These maps correspond to the quantities of the freshwater lenses left behind.

After the adjustment, the barotropic pressure signal is mostly dispersed, and the sea surface height anomaly associated with the freshwater lens can be identified from the baroclinic pressure anomaly

$$\delta h_f = -\frac{\delta\rho}{\rho_0}H_1\left(1 + \frac{\delta h}{H_1}\right) \approx \beta S_0\delta h \ll \delta h. \quad (11)$$

The salinity and sea level change due to precipitation on such relatively small scales can be estimated using the equations discussed above, as shown in Fig. 4. The results shown in this figure apply to scales much smaller than the barotropic radius of deformation, that is, for scale of hundreds of kilometers or less. For example, for an upper layer 50 m thick and $S = 35$, a rainfall of 50 cm leads to a sea surface height anomaly $\delta\eta \approx 1.35$ cm and sea surface salinity anomaly $\delta S \approx -0.3$.

In addition, in the ocean f is not constant, so these

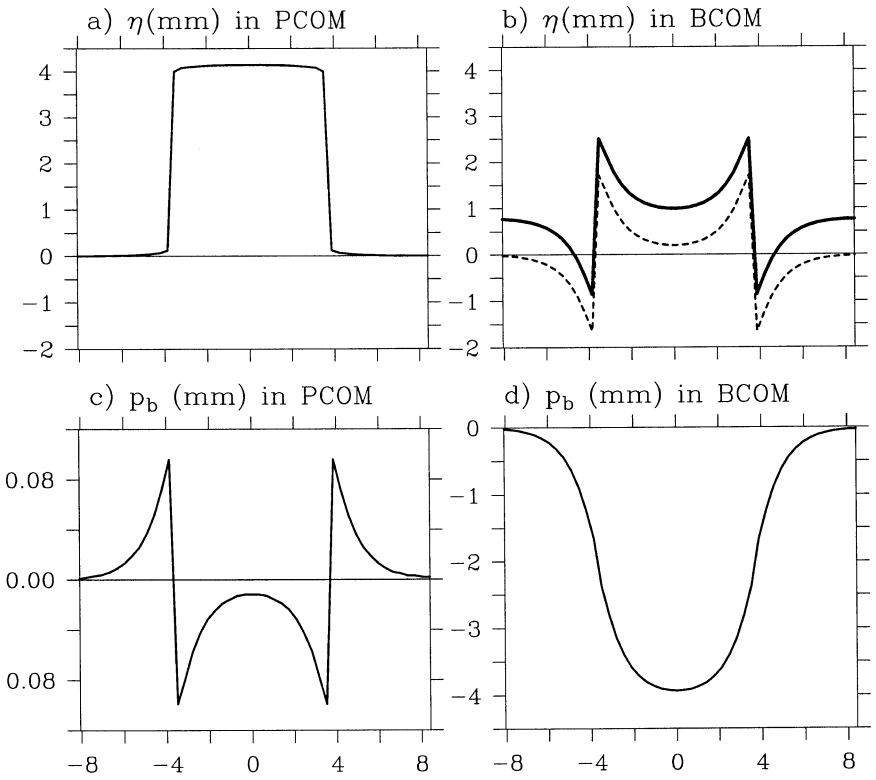

FIG. 5. Free surface elevation and bottom pressure perturbations along the midsection, diagnosed from PCOM and BCOM for the case f = const. The horizontal axis is in units of barotropic radius of deformation. The dashed line and solid line in (b) depict the free surface elevation before and after the global correction as discussed in the text.

freshwater domes and lenses are subject to strong dispersion by both barotropic and baroclinic Rossby waves. As a consequence, signals in sea surface height and bottom pressure induced by precipitation can disappear quickly into the background noise level, and they may be difficult to identify from satellite data.

5. Geostrophic adjustment of isolated features in numerical models

The theoretical analysis presented above was also confirmed using the newly developed models PCOM and BCOM. We have carried out many numerical experiments, and these results are consistent with our theoretical analysis. For the case on an f plane, the numerical solutions from both PCOM and BCOM match the analytical solutions within the truncation errors of the model.

a. Experiments forced by heating anomaly

As examples, we present a few sets of numerical experiments in this section. In most experiments, the model ocean is a simple square basin of 60° × 60°, with a modest resolution of 2° × 2° and 15 layers. The same time step, $\Delta t = 1$ h, has been used for both the baroclinic velocity and tracers.

The first experiment is carried out on the f plane, and the initial state has uniform temperature 6°C and salinity 35. To verify the analytical solution discussed above, we used a model ocean with a shallow depth of 100 m, so that the initial thermal perturbations have a horizontal scale of the barotropic radius of deformation, as shown in Fig. 5. Heating anomaly was imposed within a square of 22° × 22° in the center of the model ocean by assuming that the upper 10 m of the ocean is heating up 3°C instantaneously at $t = 0$.

The solution is illustrated by a section through the middle of the model. Because the initial horizontal scale is about 2 times as large as the barotropic radius of deformation, the initial pressure signals basically persisted, as expected from the theory of geostrophic adjustment. In fact, there is a strong sea surface elevation anomaly and very small bottom pressure signal left in the steady state in PCOM (see left-hand panels of Fig. 5). On the other hand, there are relatively small sea surface elevation and strong bottom pressure signals left in the steady state in BCOM (see right-hand panels of Fig. 5). In addition, we have applied the correction to the sea surface elevation obtained from BCOM and included it as the heavy line in Fig. 5b. Although the global adjustment does improve the solution slightly, it is obvious that such a globally uniform adjustment can-

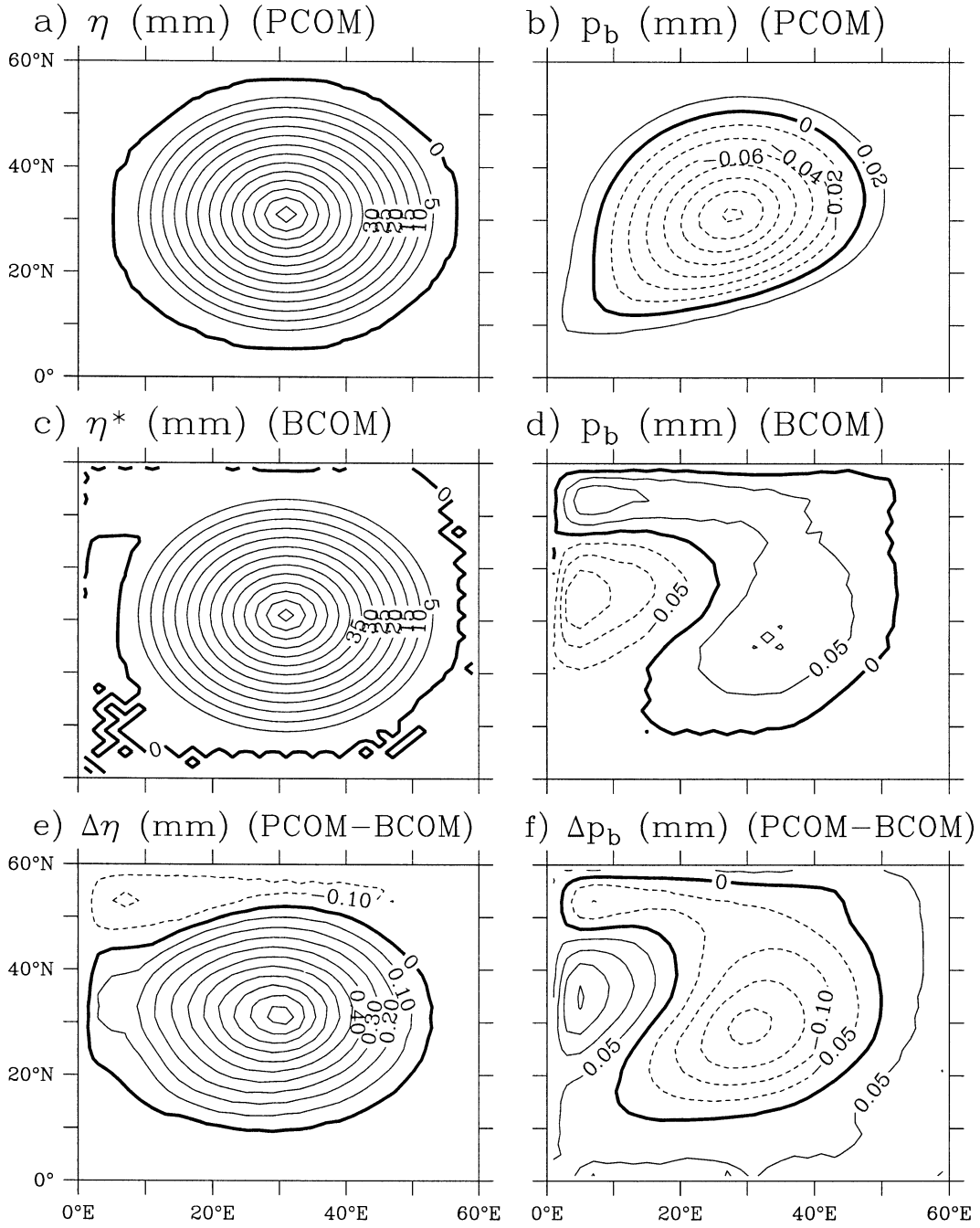

FIG. 6. The structure of the solution due to localized heating at day 50 in PCOM and BCOM for a model ocean 5 km deep (mm).

not restore the true solution. The bottom pressure profile obtained from BCOM is so much different from that obtained from PCOM that we did not include the global correction because it really would not help to improve the solution at all.

The experiment discussed above serves to verify the analytical solution and illustrates the difference in Boussinesq and non-Boussinesq models: however, this experiment greatly exaggerates the difference between PCOM and BCOM because of several factors in the setting of the experiments: 1) the ocean is too shallow, 2) there is no β effect and 3) the heating was applied within an infinitesimal time duration $\Delta t \to 0$.

To assess the potential errors in ocean models based on the Boussinesq approximations, we carried out two more experiments with more realistic settings: 1) the model ocean is 5 km deep; 2) the β effect is included because now f varies with latitude; and 3) a heat flux

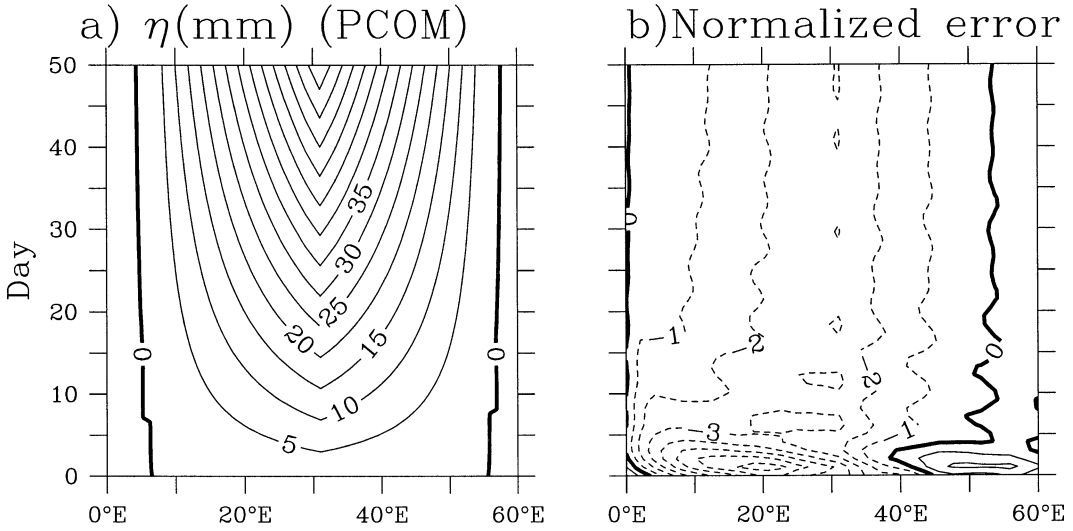

FIG. 7. Time evolution of the solution: (a) sea surface elevation in PCOM; and (b) normalized error in BCOM, defined as $(\eta^* - \eta_{\text{pcom}})/(\sqrt{\overline{\eta_{\text{pcom}}^2}^x}) \times 100\%$, where η^* is the corrected sea surface elevation in BCOM.

of 200 W m^{-2} applied within a circle with a radius of 12°, centralized at the middle of the model ocean, and the heat flux is linearly reduced to zero at the edge of the circle.

The model ocean has a constant salinity of 35 and a vertically linear temperature profile, from 0°C (on the bottom) to 25°C at the upper surface. The horizontal structure of the solution for day 50 is shown in Fig. 6. Recall that the sea surface elevation and bottom pressure presented in Figs. 6c and 6d have included the correction. Although the sea surface elevation pattern from BCOM looks similar to that from PCOM, note that PCOM predicts a sea surface elevation 1 mm higher than BCOM (Figs. 6a,c,e).

When f varies with latitude, the solution becomes much more complicated because of the dispersion associated with Rossby waves. The time evolution of the free surface elevation taken along the midsection is shown in Fig. 7. The normalized error in BCOM is the largest within the first few days, although the amplitude of the error is relatively small (Fig. 7). The errors in η move westward quickly, resembling the barotropic Rossby waves. In day 50, the relative error in sea surface elevation at the center of the heating anomaly is about 3%. Thus, the errors in each time step do accumulate and lead to errors larger than the 1%–2% based on instantaneous estimate. Furthermore, the relatively large errors during the first few days after the heating may be a source of high-frequency aliasing errors.

The bottom pressure signal from heating is expected

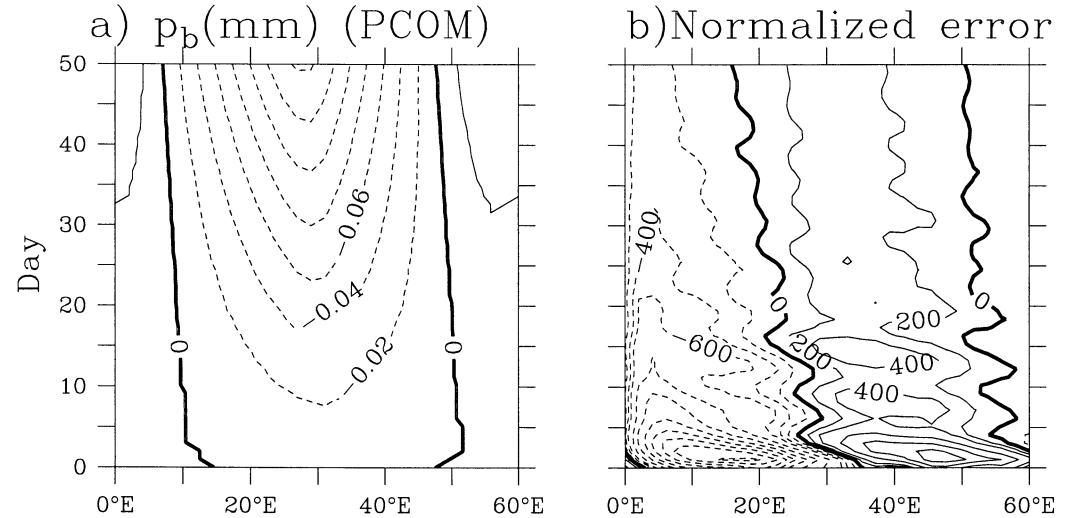

FIG. 8. Time evolution of the solutions taken along the central latitude: (a) bottom pressure in PCOM; and (b) normalized error in BCOM, defined as $(p_b^* - p_{b,\text{pcom}})/(\sqrt{\overline{p_{b,\text{pcom}}^2}^x}) \times 100\%$, where p_b^* is the corrected bottom pressure in BCOM.

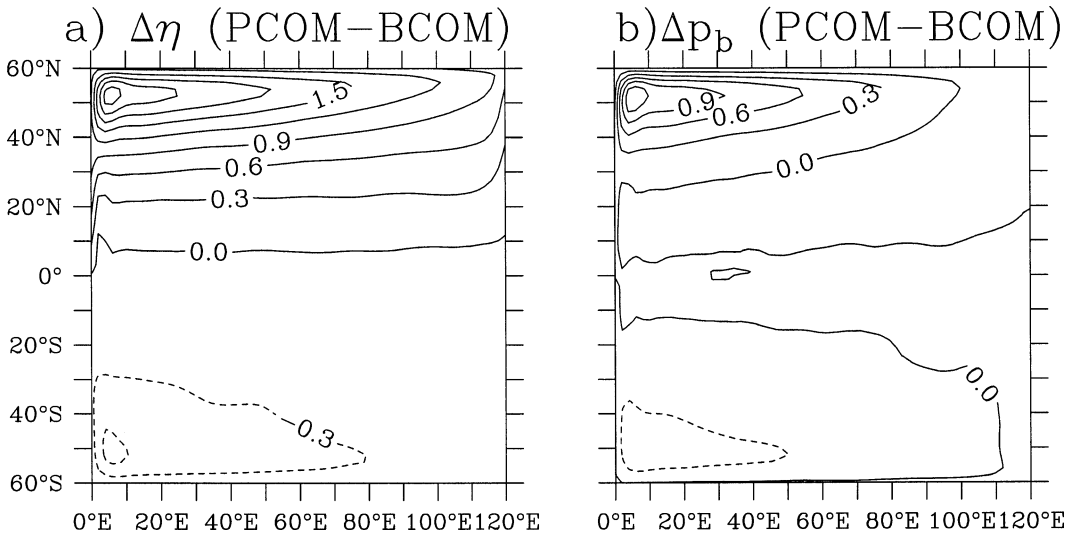

FIG. 9. Difference in (a) sea surface elevation and (b) bottom pressure between PCOM and BCOM (with the global correction) for a model ocean with heating in the northern basin at day 50 (mm).

to be small in PCOM because there is no mass flux through the air–sea interface. A small amount of water does move out the area of heating, so there is a small negative bottom pressure anomaly gradually formed locally (Fig. 6b). Such a small and negative bottom pressure anomaly in the area of heating is consistent with the theoretical argument presented in Fig. 1. On the other hand, the bottom pressure anomaly from BCOM, with correction, is totally different from that from PCOM, as shown in Figs. 6d and 6f. The maximal error is about 0.2 mm.

The temporal evolution of the bottom pressure taken along the midsection is shown in Fig. 8. Within the domain of thermal forcing anomaly, p_b in PCOM has weak and negative signals that gradually intensify (Fig. 8a). As discussed above, the global correction is necessary for BCOM before any analysis of the dynamic meaning can be done. With the global correction, the time evolution of the bottom pressure signal is dramatically different from that of the PCOM. The normalized errors associated with the bottom pressure at this section are very large. On the other hand, the bottom pressure signals produced in these numerical experiments are so small that they may not be detectable with instruments. However, reasons for the difference in bottom pressure for cases with realistic bottom topography and currents remain unclear, and it is left for further study.

To demonstrate the effect of lateral boundaries in retaining the initial perturbations, we carried out an experiment for a large basin that mimics the Pacific. The model has a dimension of 120° × 120° (from 60°S to 60°N), with a horizontal resolution of 2° × 2°. At time $t = 0$, the ocean is forced by a heating source, which is 200 W m^{-2} at 60°N and is linearly reduced to zero at the equator, with no heating in the Southern Hemisphere. The difference in both the surface elevation (2.4 mm) and bottom pressure (1.2 mm) is larger than in the previous experiment (Fig. 9). Such relatively large errors are due to the fact that the boundaries of the basin prevent a complete dispersion of the barotropic Rossby waves. As a result, part of the initial pressure perturbations is retained, so the error introduced by the Boussinesq models is more noticeable. A comprehensive examination of the dynamic effects of the lateral boundaries and topography is left for further study.

b. Experiments forced by precipitation

The dynamic effect of precipitation in the ocean is more complicated. As discussed above, precipitation induces barotropic pressure perturbations that excite barotropic Rossby waves. Because barotropic waves travel quickly, the barotropic pressure signals disperse over the ocean within the order of one week. Because of the finite dimensions of the ocean, waves reflect and travel back to the eastern boundary via the edge of the basin as Kelvin waves and move westward again in the form of Rossby waves in the ocean interior. As a result, the perturbations induced by precipitation are dominated by strong barotropic Rossby waves.

Three experiments were carried out with a square basin of 50° × 50°, with 1° × 1° resolution. In the first experiment, the model ocean is shallow, with a depth of 1 km, with 15 layers of uneven thickness. The PCOM model was started from a rest ocean with 50 mm of precipitation at the surface over one day within a square of 11° at the center of the basin. The central latitude is 25°N, and the initial horizontal scale of the perturbation is $R = 0.33$, in units of the radius of barotropic deformation.

In the second experiment, the model ocean is 5 km deep, with 15 layers of uneven thickness, and PCOM

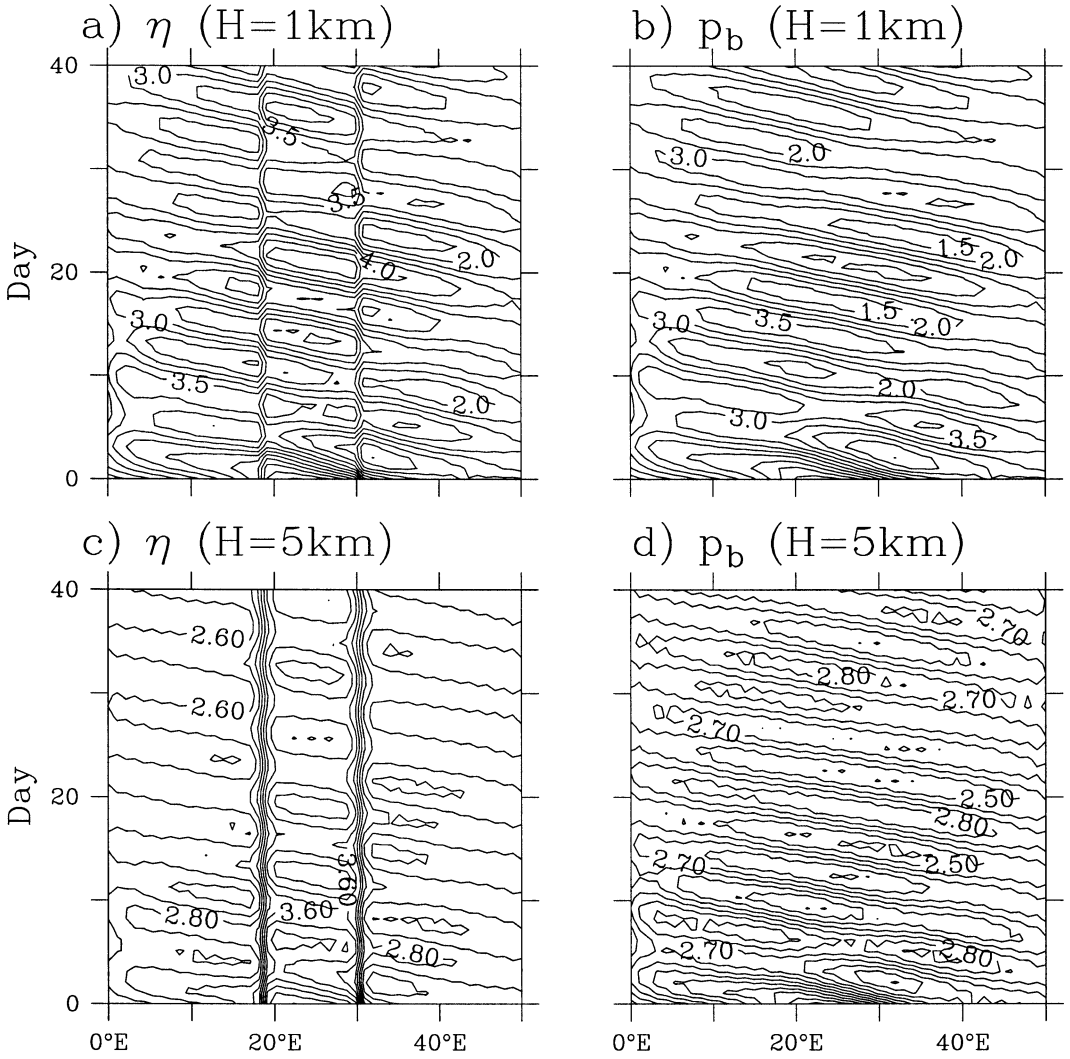

FIG. 10. The time evolution of sea surface elevation and bottom pressure anomaly (PCOM) from precipitation of 5 cm accumulated over one day, taken along the central latitude of the precipitation (mm).

was used. The top layer initially has a thickness equivalent to 22 m of water, and the lowest layer has a thickness equivalent to 645 m of water. The initial horizontal scale of the perturbation is $R = 0.15$, in units of the barotropic radius of deformation. In the third experiment, we run BCOM under the virtual salt flux condition (VSF) with the same model settings as used in the second experiment.

For the case of a shallow model ocean with $R = 0.33$, the horizontal scale of the initial perturbations is smaller than the barotropic radius of deformation, and the initial sea surface elevation and bottom pressure signals are mostly lost during the process of geostrophic adjustment, which takes 2 days. As seen from Figs. 10a and 10b, the amplitude of sea surface elevation and bottom pressure is on the order of 6 mm, more than 10% of the total precipitation (50 mm).

On the other hand, for the case of a deep ocean with $R = 0.15$, the horizontal scale of the initial perturbations is much smaller than the barotropic radius of deformation, so the dispersion of the initial sea surface elevation and bottom pressure signals are more complete than in the previous case. As seen from Figs. 10c and 10d, the amplitude of sea surface elevation and bottom pressure is on the order of 3 mm, about 6% of the total precipitation. Thus, these solutions obtained at the end of the fast geostrophic adjustment are consistent with our theoretical analysis presented in Section 4.

Because these experiments were carried out on model-based spherical coordinates, the evolution of the solution after the relatively fast geostrophic adjustment is controlled by the Rossby waves. For the case of a shallow ocean ($R = 0.33$), the perturbations have a relatively large amplitude and the phase speed of the Rossby waves is relatively slow. Because the space occupied by the model ocean is finite, energy carried by the waves

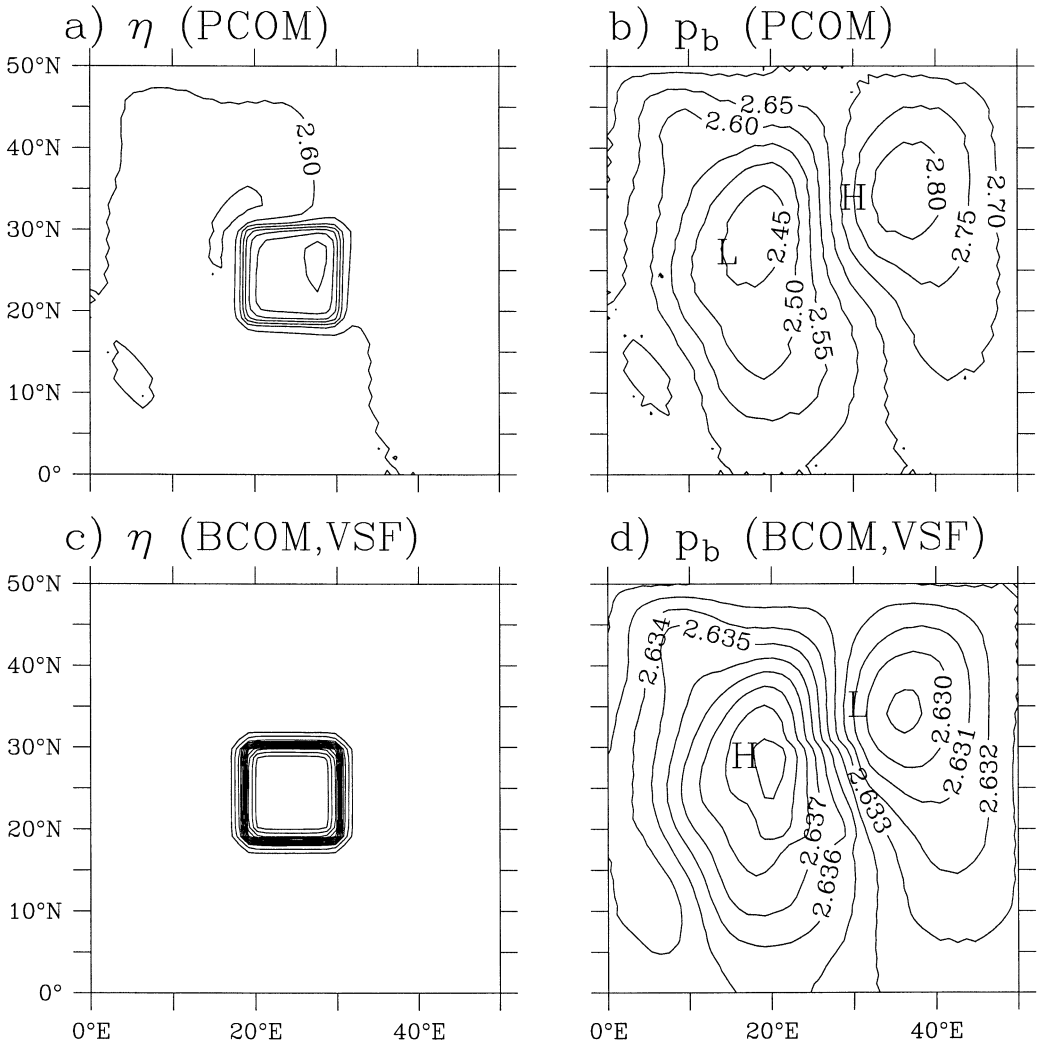

FIG. 11. The sea surface elevation and bottom pressure anomaly (at day 30) from precipitation of 5 cm over a 5-km deep ocean (mm). Note that BCOM was run under the virtual salt flux condition and the global correction has been applied to both the sea surface elevation and bottom pressure.

cannot disperse into infinity; instead, these energy-contained waves reflect back from the western boundary in the form of Kelvin waves that propagate along the edge of the model basin and radiate from the eastern boundary. As a result, strong barotropic Rossby waves excited by the precipitation slosh back and forth, as seen from Figs. 10a and 10b.

For the case with a deep ocean ($R = 0.15$), the initial scale of the perturbations is much smaller than the barotropic radius of deformation, so they quickly disperse through barotropic Rossby waves and leave behind a sea surface height anomaly around the center of the perturbation. The freshwater lens behind after the completion of geostrophic adjustment is very close to the theoretical limit discussed in the previous section; that is, there is very little bottom pressure signal left, but the sea surface height anomaly left is very close to that calculated from Eq. (11), as depicted by the solid lines in Figs. 10c and 10d.

The horizontal structure of the solutions at day 30 is shown in Fig. 11. The baroclinic pressure signal is outstanding in the sea surface elevation pattern but not in the bottom pressure pattern (Figs. 11a and 11b). As discussed above, the barotropic pressure signal associated with precipitation is mostly lost during the geostrophic adjustment, and what is left are small-amplitude perturbations that propagate as Rossby waves (see Figs. 11a,b and Figs. 12a,b).

c. Experiments forced by virtual salt flux

Here we discuss the pitfalls of using VSF. Although VSF is not part of the Boussinesq approximations, over a long time VSF has been used in many studies. Part

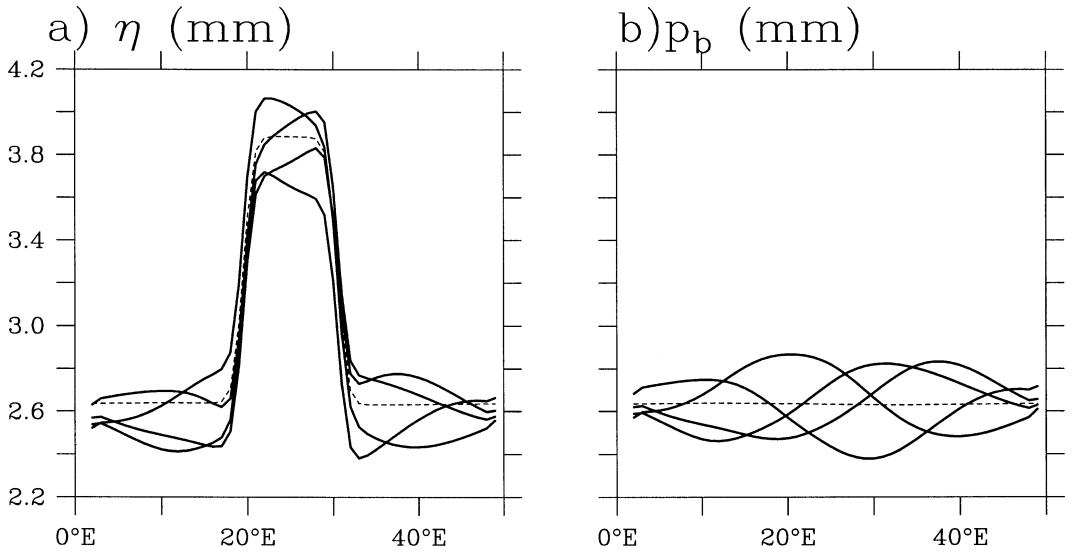

FIG. 12. The sea surface height and bottom pressure taken at the central latitude of the precipitation at days 31, 33, 35, and 37: the solid lines are for PCOM and the dashed lines are for BCOM (under the virtual salt flux condition).

of the reason for using VSF is that an accurate precipitation and evaporation dataset is not available for many applications. However, using VSF may induce noticeable errors in the simulation of free surface and bottom pressure. We have carried out the third experiment to illustrate the pitfalls of using VSF in numerical simulation. The BCOM is run under a virtual salt flux that is equivalent to 50 mm of precipitation over one day. (The same experiment can be carried out with the PCOM and VSF, with almost identical results.) The model setting is exactly the same as in the second experiment discussed above, that is, an ocean that is 5 km deep.

As in the previous cases, the global correction was applied to results from this run before any analysis. Both the sea surface elevation and bottom pressure pattern at day 30 are shown in Figs. 11c and 11d. Although the patterns for PCOM and BCOM + VSF look similar, a close examination reveals that the spatial gradient of both η and p_b in BCOM + VSF is much smaller than that in PCOM. In fact, the spatial gradient of η and p_b in BCOM + VSF is so small (the η field in BCOM + VSF consists of two zones of constant value linked by a sharp front) that we do not included them in Fig. 10. The η and p_b taken along the central latitude of precipitation from PCOM and BCOM + VSF are shown in Fig. 12.

The essential difference in these two cases is the following: For a model under VSF, the additional mass from precipitation is totally neglected. Furthermore, the reduction of salinity due to the equivalent salt flux induces a mass loss in the model, $\rho_0\beta S_0\delta h \approx 0.025\rho_0\delta h$. Thus, the precipitation is simulated with a barotropic pressure signal that is much smaller and has a wrong sign. During the geostrophic adjustment this barotropic pressure signal is mostly lost for the case of a deep ocean, so the amplitude of the barotropic Rossby waves associated with the residual of the barotropic pressure is extremely small; see Figs. 11c and 11d. A careful examination reveals that the bottom signal in BCOM has sign opposite to that in PCOM, and this result is consistent with the reasoning above that the positive mass gain from precipitation is replaced by a mass loss (of much smaller amplitude).

Similar to the case with the natural boundary condition, there is a baroclinic signal associated with the relatively low salinity water in the upper box. Because the initial scale of the perturbations is much larger than the baroclinic radius of deformation, the baroclinic pressure signals persist. Thus, a small positive sea level signal (associated with the initial baroclinic pressure signal) and a zero bottom pressure signal remain. With the global correction, this is what the dashed lines in Fig. 12 indicate. In summary, the model under VSF neglects the mass contribution from precipitation and evaporation; instead, there is a negative mass source from freshening in the upper layer. Thus, the barotropic Rossby waves associated with precipitation and evaporation are simulated incorrectly in such model runs.

It is important to note that because precipitation generates barotropic Rossby waves that can cross the ocean in less than 10 days, these waves may be difficult to analyze using satellite data collected over a time interval longer than 10 days.

6. Conclusions

Boussinesq approximations have been commonly used in both theoretical and numerical models. These approximations have been proven to be accurate for many applications. However, errors introduced by these approximations may not be totally negligible. In this study, we have shown that these approximations distort

the physical processes in the oceans and thus lead to noticeable errors in the time evolution and the equilibrium state of the free surface and bottom pressure. The errors introduced by the Boussinesq approximations were studied using geostrophic scaling, the theory of geostrophic adjustment under simple geometry, and a newly developed PCOM model. Results from these three approaches lead to consistent estimates for the possible errors induced by these approximations.

The largest errors associated with the Boussinesq approximations appear when the ocean is subject to strong thermal forcing on large scales (on the order of thousands of kilometers). Because of the artificial source/sink of mass in the Boussinesq models, the free surface elevation and bottom pressure signals induced by thermal forcing produced from these models may be noticeably different from those obtained from the truly non-Boussinesq models. In a similar way, using the virtual salt flux condition can induce noticeable errors caused by omitting the barotropic Rossby waves induced by precipitation and evaporation.

The Boussinesq approximations have dominated oceanic circulation modeling for the past century. We hope that with fast advances in new technology, including high-accuracy satellite missions, such as the Ocean Topography Experiment (TOPEX) and the Gravity Recovery and Climate Experiment (GRACE), and increasingly speedy microchips, mass-conserving models may become more widely used in the near future.

Acknowledgments. We thank Drs. J. Pedlosky and X.-H. Zhang for their suggestions and criticism through this study. Comments from two reviewers were very helpful in improving the presentation. R. X. H. was supported by the National Science Foundation through Grant OCE9616950 and a Mellor Independent Study Award (WHOI). Author X. J. was supported by a Mellor Independent Study Award (WHOI) and the National Science Foundation of China through Grant 49875010.

APPENDIX

Geostrophic Adjustment Induced by Initial Density Perturbations

The geostrophic adjustment of a multilayer model in the ocean has been discussed in many papers, for example, Stommel and Veronis (1980). Our analysis here parallels that by Mihaljan (1963). If one assumes the flow field is independent of x, the x-momentum equations are

$$\frac{du_1}{at} = fv_1 \quad \text{and} \quad \frac{du_2}{dt} = fv_2.$$

Upon integration from $t = 0$ to ∞, these lead to

$$u_1 = f(y - Y_1) + U_1(Y_1) \quad \text{and}$$

$$u_2 = f(y - Y_2) + U_2(Y_2),$$

where Y_1 and Y_2 are the initial positions of the water parcels and U_1 and U_2 are the initial velocities. In the final state, the downstream velocities are geostrophic:

$$fu_1 = -g(h_{1y} + h_{2y}) \quad \text{and} \quad fu_2 = -g(\gamma h_{1y} + h_{2y}),$$

where $\gamma = (\rho - \delta\rho)/\rho < 1$. Conservation of mass in each layer gives

$$h_1 = H_1\frac{dY_1}{dy} \quad \text{and} \quad h_2 = H_2\frac{dY_2}{dy},$$

where H_1 and H_2 are the initial layer thickness.

These equations can be solved for the cases of simple geometry, such as a semi-infinite plane or a patch of density perturbation due to thermohaline forcing on an f plane. Since the solution is symmetric with respect to center, we will discuss the right-hand-side half of the solution. The half-width of the original density patch is ΔY, and the final solution consists of three segments as shown in Fig. A1b.

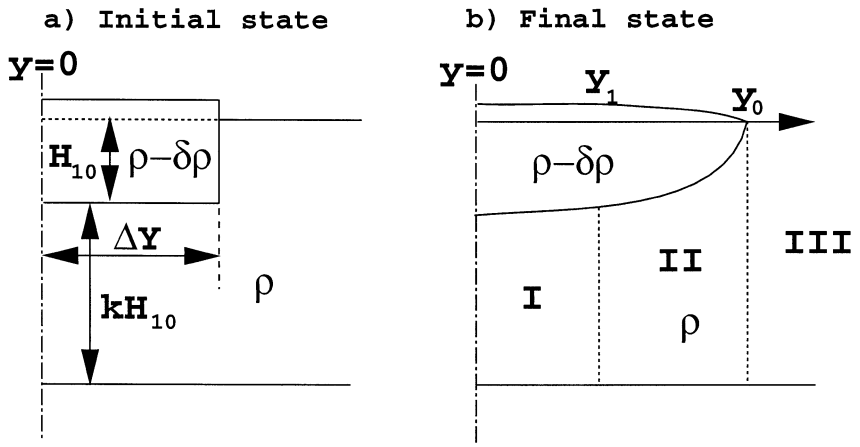

FIG. A1. Sketch of the geostrophic adjustment in a two-layer model ocean.

a. Region I

Region I is $0 \le y \le y_1$, where both layers are in motion. The unperturbed depths of the first and second layers are $\chi H_{1\infty}$ and $\kappa H_{1\infty}$, $\chi = 1$ for heating in a Boussinesq model, $\chi = 1/\gamma$ for heating in a compressible model, and $\chi = p/\gamma$ for precipitation in a compressible model. (Here $p - 1$ indicates the contribution from precipitation.) To facilitate the analysis, we introduce the nondimensional variables

$$h_1 = H_{1\infty} h_1', \qquad h_2 = \kappa H_{1\infty} h_2', \qquad y = \frac{\sqrt{gH_{1\infty}}}{f} y',$$
$$U_1 = \sqrt{gH_{1\infty}}\, u_{10}', \quad \text{and} \quad U_2 = \sqrt{gH_{1\infty}}\, u_{20}'.$$

In this study, we will discuss the cases of an initially stagnant ocean, so the initial velocity is zero; for the case with nonzero velocity, see Huang (1990). Using these nondimensional variables and dropping the primes, we derive two second-order ordinary differential equations

$$\chi \frac{d^2 Y_1}{dy^2} + \kappa \frac{d^2 Y_2}{dy^2} - Y_1 = -y$$
$$\gamma\chi \frac{d^2 Y_1}{dy^2} + \kappa \frac{d^2 Y_2}{dy^2} - Y_2 = -y.$$

Their solutions are

$$Y_1^{\mathrm{I}} = y + a_1 e^{\alpha_+ y} + a_2 e^{-\alpha_+ y} + a_3 e^{\alpha_- y} + a_4 e^{-\alpha_- y},$$
$$Y_2^{\mathrm{I}} = y + b_1 e^{\alpha_+ y} + b_2 e^{-\alpha_+ y} + b_3 e^{\alpha_- y} + b_4 e^{-\alpha_- y},$$
$$h_1 = 1 + a_1\alpha_+ e^{\alpha_+ y} - a_2\alpha_+ e^{-\alpha_+ y} + a_3\alpha_- e^{\alpha_- y} - a_4\alpha_- e^{-\alpha_- y},$$
$$h_2 = 1 + b_1\alpha_+ e^{\alpha_+ y} - b_2\alpha_+ e^{-\alpha_+ y} + b_3\alpha_- e^{\alpha_- y} - b_4\alpha_- e^{-\alpha_- y},$$

where

$$\alpha_\pm = \left[\frac{\kappa + \chi \pm \sqrt{(\kappa - \chi)^2 + 4\kappa\gamma\chi}}{2\kappa\chi(1 - \gamma)}\right]^{1/2}.$$

b. Region II

Region II is $y_1 \le y \le y_0$, where both layers are in motion, the unperturbed depth of the first layer is χ, and the unperturbed depth of the second layer is $\kappa + 1$. The basic equations are

$$\chi \frac{d^2 Y_1}{dy^2} + (\kappa + 1)\frac{d^2 Y_2}{dy^2} - Y_1 = -y,$$
$$\gamma\chi \frac{d^2 Y_1}{dy^2} + (\kappa + 1)\frac{d^2 Y_2}{dy^2} - Y_2 = -y,$$

$$Y_1^{\mathrm{II}} = y + c_1 e^{\beta_+ y} + c_2 e^{-\beta_+ y} + c_3 e^{\beta_- y} + c_4 e^{-\beta_- y},$$
$$Y_2^{\mathrm{II}} = y + d_1 e^{\beta_+ y} + d_2 e^{-\beta_+ y} + d_3 e^{\beta_- y} + d_4 e^{-\beta_- y},$$
$$h_1^{\mathrm{II}} = 1 + c_1\beta_+ e^{\beta_+ y} - c_2\beta_+ e^{-\beta_+ y} + c_3\beta_- e^{\beta_- y} - c_4\beta_- e^{-\beta_- y},$$
$$h_2^{\mathrm{II}} = 1 + d_1\beta_+ e^{\beta_+ y} - d_2\beta_+ e^{-\beta_+ y} + d_3\beta_- e^{\beta_- y} - d_4\beta_- e^{-\beta_- y},$$

where

$$\beta_\pm = \left[\frac{\kappa + 1 + \chi \pm \sqrt{(\kappa + 1 - \chi)^2 + 4(\kappa + 1)\gamma\chi}}{2(\kappa + 1)\chi(1 - \gamma)}\right]^{1/2}.$$

c. Region III

Region III is $y_0 \le y$, where the upper layer vanishes, and only the lower layer is in motion, with the nondimensional unperturbed thickness of $\kappa + 1$. The basin equation is

$$(\kappa + 1)\frac{d^2 Y_2}{dy^2} - Y_2 = -y.$$

The solution is

$$Y_2^{\mathrm{III}} = y + e_1 e^{-\mu y}, \quad \text{and} \quad h_2^{\mathrm{III}} = 1 - e_1\mu e^{-\mu y},$$

where $\mu = [1/(\kappa + 1)]^{1/2}$.

There are 19 unknown constants: a_1, a_2, a_3, a_4, b_1, b_2, b_3, b_4, c_1, c_2, c_3, c_4, d_1, d_2, d_3, d_4, e_1, y_0, and y_1. To determine these constants we use the following constraints. The basic equations in Region I require

$$b_1 = \frac{\gamma\chi\alpha_+^2}{1 - \kappa\alpha_+^2} a_1, \qquad b_2 = \frac{\gamma\chi\alpha_+^2}{1 - \kappa\alpha_+^2} a_2,$$
$$b_3 = \frac{\gamma\chi\alpha_-^2}{1 - \kappa\alpha_-^2} a_3, \qquad b_4 = \frac{\gamma\chi\alpha_-^2}{1 - \kappa\alpha_-^2} a_4,$$
$$d_1 = \frac{\gamma\chi\beta_+^2}{1 - (\kappa + 1)\beta_+^2} c_1, \qquad d_2 = \frac{\gamma\chi\beta_+^2}{1 - (\kappa + 1)\beta_+^2} c_2,$$
$$d_3 = \frac{\gamma\chi\beta_-^2}{1 - (\kappa + 1)\beta_-^2} c_3,$$
$$d_4 = \frac{\gamma\chi\beta_-^2}{1 - (\kappa + 1)\beta_-^2} c_4.$$

The continuity of the solution at y_1 requires

$$a_1 e^{\alpha_+ y_1} + a_2 e^{-\alpha_+ y_1} + a_3 e^{\alpha_- y_1} + a_4 e^{-\alpha_- y_1}$$
$$= c_1 e^{\beta_+ y_1} + c_2 e^{-\beta_+ y_1} + c_3 e^{\beta_- y_1} + c_4 e^{-\beta_- y_1},$$
$$b_1 e^{\alpha_+ y_1} + b_2 e^{-\alpha_+ y_1} + b_3 e^{\alpha_- y_1} + b_4 e^{-\alpha_- y_1}$$
$$= d_1 e^{\beta_+ y_1} + d_2 e^{-\beta_+ y_1} + d_3 e^{\beta_- y_1} + d_4 e^{-\beta_- y_1},$$
$$a_1 \alpha_+ e^{\alpha_+ y_1} - a_2 \alpha_+ e^{-\alpha_+ y_1} + a_3 \alpha_- e^{\alpha_- y_1} - a_4 \alpha_- e^{-\alpha_- y_1}$$
$$= c_1 \beta_+ e^{\beta_+ y_1} - c_2 \beta_+ e^{-\beta_+ y_1} + c_3 \beta_- e^{\beta_- y_1} - c_4 \beta_- e^{-\beta_- y_1},$$

and

$$\kappa(1 + b_1 \alpha_+ e^{\alpha_+ y_1} - b_2 \alpha_+ e^{-\alpha_+ y_1} + b_3 \alpha_- e^{\alpha_- y_1} - b_4 e^{-\alpha_- y_1})$$
$$= (\kappa + 1)(1 + d_1 \beta_+ e^{\beta_+ y_1} - d_2 \beta_+ e^{-\beta_+ y_1} + d_3 \beta_- e^{\beta_- y_1}$$
$$- d_4 \beta_- e^{\beta_- y_1}).$$

The continuity of the solution at $y = y_0$ requires

$$d_1 e^{\beta_+ y_0} + d_2 e^{-\beta_+ y_0} + d_3 e^{\beta_- y_0} + d_4 e_4^{-\beta_- y_0}$$
$$= e_1 e^{-\mu y_0},$$
$$d_1 \beta_+ e^{\beta_+ y_0} - d_2 \beta_+ e^{-\beta_+ y_0} + d_3 \beta_- e^{\beta_- y_0} - d_4 \beta_- e^{-\beta_- y_0}$$
$$= -e_1 \mu e^{-\mu y_0}.$$

In addition, the upper layer vanishes at $y = y_0$:

$$c_1 \beta_+ e^{\beta_+ y_0} - c_2 \beta_+ e^{-\beta_+ y_0} + c_3 \beta_- e^{\beta_- y_0} - c_4 \beta_- e^{-\beta_- y_0}$$
$$= -1.$$

At the origin the particles do not move, so $Y_1 = Y_2 = 0$ at $y = 0$:

$$a_1 + a_2 + a_3 + a_4 = 0, \quad \text{and} \quad b_1 + b_2 + b_3 + b_4 = 0.$$

Last, the fronts in layers 1 and 2 should be the same in the old coordinates, ΔY:

$$y_0 + c_1 e^{\beta_+ y_0} + c_2 e^{-\beta_+ y_0} + c_3 e^{\beta_- y_0} + c_4 e^{-\beta_- y_0}$$
$$= y_1 + b_1 e^{\alpha_+ y_1} + b_2 e^{-\alpha_+ y_1} + b_3 e^{\alpha_- y_1} + b_4 e^{-\alpha_- y_1}$$

and

$$y_0 + c_1 e^{\beta_+ y_0} + c_2 e^{-\beta_+ y_0} + c_3 e^{\beta_- y_0} + c_4 e^{-\beta_- y_0}$$
$$= \Delta Y.$$

These equations are linear in a_1, a_2, a_3, a_4, b_1, b_2, b_3, b_4, c_1, c_2, c_3, c_4, d_1, d_2, d_3, d_4, and e_1. Thus, after eliminating these constants, we obtain two transcendental equations of two unknowns y_0 and y_1.

REFERENCES

Bois, P. A., 1991: Asymptotic aspects of the Boussinesq approximation for gases and liquids. *Geophys. Astrophys. Fluid Dyn.*, **58,** 45–55.

Boussinesq, J., 1903: *Théorie Analytique de la Chaleur.* Vol. 2. Gathier-Vellars, 172 pp.

Bryan, F., 1997: The axial angular momentum balance of a global ocean general circulation model. *Dyn. Atmos. Oceans,* **25,** 191–216.

Dukowicz, J. K., 1997: Steric sea level in the Los Alamos POP code—Non-Boussinesq effects. *Numerical Methods in Atmospheric and Oceanic Modelling: The Andre Robert Memorial Volume,* C. A. Lin, R. Laprise, and H. Ritchie, Eds., Can. Meteor. Oceanogr. Soc., 534–546.

Greatbatch, R. J., 1994: A note on the representation of steric sea level in models that conserve volume rather than mass. *J. Geophys. Res.,* **99,** 12 767–12 771.

Huang, R. X., 1990: Does atmospheric cooling drive the Gulf Stream recirculation? *J. Phys. Oceanogr.,* **20,** 750–757.

——, 1993: Freshwater flux as a natural boundary condition for the salinity balance and thermohaline circulation forced by evaporation and precipitation. *J. Phys. Oceanogr.,* **23,** 2428–2446.

——, X.-Z. Jin, and X.-H. Zhang, 2001: An oceanic general circulation model in pressure coordinates. *Adv. Atmos. Sci.,* **18,** 1–22.

Jackett, D. R., and T. J. McDougall, 1995: Stabilization of hydrographic data. *J. Atmos. Oceanic Technol.,* **12,** 381–389.

Mellor, G. L., and T. Ezer, 1995: Sea level variations induced by heating and cooling: An evaluation of the Boussinesq approximation in ocean models. *J. Geophys. Res.,* **100,** 20 565–20 577.

Mihaljan, J. M., 1962: A rigorous derivation of the Boussinesq approximation applicable to a thin layer of fluid. *Astrophys. J.,* **136,** 1126–1133.

——, 1963: An exact solution of the Rossby adjustment problem. *Tellus,* **15,** 150–154.

Pedlosky, J., 1987: *Geophysical Fluid Dynamics.* Springer-Verlag, 710 pp.

Ponte, R. M., 1999: A preliminary model study of the large-scale seasonal cycle in bottom pressure over the global ocean. *J. Geophys. Res.,* **104,** 1289–1300.

Rossby, C. G., 1938: On the mutual adjustment of pressure and velocity distributions in certain simple current systems, II. *J. Mar. Res.,* **1,** 239–263.

Spiegel, E. A., and G. Veronis, 1960: On the Boussinesq approximation for a compressible fluid. *Astrophys. J.,* **131,** 442–447.

Stommel, H., and G. Veronis, 1980: Barotropic response to cooling. *J. Geophys. Res.,* **85,** 6661–6666.

Wolfgang, K., 1973: *Dynamics of the Homogeneous and the Quasi-Homogeneous Ocean.* Gebruder Borntraeger, 302 pp.

Yeh, T. C., 1957: On the formation of quasi-geostrophic motion in the atmosphere. *J. Meteor. Soc. Japan,* **36,** 130–134.

Zeytounian, R. K., 1989: The Benard problem for deep convection: Rigorous derivation of approximate motions. *Int. J. Eng. Sci.,* **27,** 1361–1366.